A Spatially Progressive Neural Network for Locally/Globally Prioritized TDLAS Tomography

A Spatially Progressive Neural Network for Locally/Globally Prioritized TDLAS Tomography

Jingjing Si, *Member*, *IEEE*, Gengchen Fu, Xin Liu, Yinbo Cheng, Rui Zhang, Jiangnan Xia, Yalei Fu, Godwin Enemali, *Member*, *IEEE*, and Chang Liu, *Senior Member, IEEE*

***Abstract*—Tunable diode laser absorption spectroscopy tomography (TDLAST) has been widely applied for imaging two-dimensional distributions of industrial flow-field parameters, e.g., temperature and species concentration. Two main interested imaging objectives in TDLAST are the local combustion and its radiation in the entire sensing region. State-of-the-art algorithms were developed to retrieve either of the two objectives. In this paper, we address the both by developing a novel multi-output imaging neural network, named as Spatially Progressive Neural Network (SpaProNet). This network consists of locally and globally prioritized reconstruction stages. The former enables hierarchical imaging of the finely resolved and highly accurate local combustion, but coarsely resolved background. The later retrieves a fine-resolved image for the entire sensing region, at the cost of slightly trading off the reconstruction accuracy in the combustion zone. Furthermore, the proposed network is driven by the hydrodynamics of the real reactive flows, in which the training dataset is obtained from large eddy simulation. The proposed SpaProNet is validated by both simulation and lab-scale experiment. In all test cases, the visual and quantitative metric comparisons show that the proposed SpaProNet outperforms the existing methods from the following two perspectives: a) the locally prioritized stage provides ever-better accuracy in the combustion zone; b) the globally prioritized stage shows turbulence-indicative accuracy in the entire sensing region for diagnosis of heat radiation from the flame and flame-air interactions.**

***Index Terms*—laser imaging, neural network, spatial resolution, tomography, tunable diode laser absorption spectroscopy.**

This work was supported in part by Hebei Natural Science Foundation under Grant F2021203027, the U.K. Engineering and Physical Science Research Council under Platform Grant EP/P001661/1, the Cultivation Project for Basic Research and Innovation of Yanshan University under Grant 2021LGZD011, and the Hebei Key Laboratory Project under Grant 202250701010046. (Corresponding author: Chang Liu)

J. Si, G. Fu and X. Liu are with the School of Information Science and Engineering, Yanshan University, Qinhuangdao 066004, China.

Y. Cheng is with the Ocean College, Hebei Agricultural University, Qinhuangdao 066003, China.

R. Zhang, J. Xia, Y. Fu, and C. Liu are with the School of Engineering, University of Edinburgh, Edinburgh EH9 3JL, U.K. (e-mail: C.Liu@ed.ac.uk)

G. Enemali is with the Department of Electrical and Electronic Engineering, Glasgow Caledonian University, Glasgow, U.K.

I. Introduction

INDUSTRIAL process tomography has been well known for non-intrusive visualization and quantification of the flow behaviors. The electrical imaging modalities are generally used to image permittivity and/or inductivity [1-3]. In contrast, Tunable Diode Laser Absorption Spectroscopy Tomography (TDLAST) offers unique capability for characterizing the thermochemical parameters, such as temperature and species concentration in reactive flows [4-6]. TDLAST is implemented in a manner analogous to X-ray tomography. Instead of using rotational X-ray sources, TDLAST collects projection data using laser beams. Taking the reliability and safety into consideration, industrial chambers and reactors are generally available for very limited optical windows. Compared with X-ray tomography that can acquire thousands of projection data from 360-degree rotation of the X-ray source, only a small number of fixed-position laser beams can access the sensing region through these windows. Consequently, the inverse problem of TDLAST is inherently ill-posed, due to the limited number of projection data and severe rank deficiency [7].

To solve the inverse problem of TDLAST, computational tomographic algorithms, such as the algebraic techniques [8] and regularization methods [9] generally mitigate the artefacts in the reconstruction by imposing implicit empirically determined penalization. Apart from non-negativity and smoothness of the reconstruction, most penalizing prior are implicit and unable to indicate the physical features of the reactive flow. The recently developed statistical inversions use explicit prior [10-13], such as linear elements, leading to highly resolved imaging of the energy-containing scales of turbulence. However, its universality may need to be further expanded since hydrodynamic features may not be adequately covered in case of isotropic turbulences with strong shear force and compressibility. In addition, the computational method suffers from complex and time-consuming computation, which hinders rapid feedback to the combustion engineers in case of high imaging rate and/or long-time test campaigns.

The fast-booming deep neural networks, especially with hardware acceleration [14], offer speedy tools for TDLAST image reconstruction. Pioneering algorithms based on Convolutional Neural Network (CNN) [15, 16] were proposed for TDLAST sensors with dense-beam layout. In recent years, an improved CNN-aided tomographic algorithm [17], a Long

Short-term Memory (LSTM) based tomographic algorithm [18], and a Swin Transformer based tomographic algorithm [19] were demonstrated on more practical TDLAST sensors with a small number of laser beams. However, all these data-driven methods are only capable of reconstructing the predetermined Region of Interest (RoI) with fixed resolution.

The choice of RoI, where distributions of flow-field parameters are to be retrieved, and the discretization schemes employed in the RoI are key factors affecting the imaging accuracy, efficiency and applicable scenarios. In general, high measurement sensitivity is enabled in the combustion zone where laser beams densely pass through. Defining the RoI as the entire sensing region with fine meshes generally introduces more artefacts in the background where is insufficiently covered by lasers beams. On the contrary, if the combustion zone is only chosen as the RoI, the imaging quality can be improved but at the cost of losing background information. Recent attempts have been made by hybrid meshing, i.e., fine meshes in the combustion zone and coarse meshes in the background, to maintain the physical integrity of laser measurement and mitigate the rank deficiency [20, 21]. However, the coarsely meshed background suffers from degenerated efficacy that is important to understand the heat radiation and flame-air interactions in many applications, such as imaging of the aero-engine exhaust [22]. Therefore, a data-driven algorithm is highly demanded for TDLAST which can optionally prioritize the reconstruction accuracy in (a) the combustion zone to highlight the physiochemical performance in the flames or (b) the global image to indicate both the flames and their nearby reactions.

To meet the above-mentioned requirements, a novel multiple-output imaging neural network, named as Spatially Progressive Neural Network (SpaProNet), is developed for TDLAST. The locally prioritized reconstruction of the combustion zone is to highlight the flame-central temperature profiles, while the globally prioritized reconstruction of the entire sensing region is to finely retrieve the characterization of heat radiation from the flame and flame-air interactions. The main contributions are:

a) A Local-Prior-Global-Progressive (LPGP) discretization is designed to enable finely resolved imaging of the combustion zone and, meanwhile, establish progressive discretization of the global image with coarse-to-fine spatial correspondence.
b) Based on the LPGP discretization, the SpaProNet is developed for temperature imaging in a locally/globally selective manner. It contains a locally prioritized stage to reconstruct high-accuracy combustion zone, and a globally prioritized stage to finely retrieve the entire sensing region.
c) The proposed SpaProNet is driven by the hydrodynamics of the real reactive flows, which is obtained from large eddy simulation. It enables better generalizability and wider applicability with minimum penalizing coefficients.
d) An experiment is designed with limited projection data to validate the SpaProNet. This indicates feasibility of the proposed network for imaging similar combustion processes in energy-generation industry, which is of great practical significance.

II. Mathematical Background

In this work, we consider the inverse problem of TDLAST to reconstruct two-dimensional (2-D) distributions of critical gas parameters from Line-of-Sight (LoS) measurements with a limited number.

If the sensing region is uniformly discretized into M grids and gas parameters in each grid are assumed to be uniform [5], as shown in Fig.1, the path integrated absorbance of the kth laser beam passing through the sensing region at the transition v, $A_{v,k}$ [cm^{-1}], can be written as

$$A_{v,k}=\sum_{m=1}^{M}a_{v,m}L_{k,m}=\sum_{m=1}^{M}\left[PX_mS_v(T_m)\right]L_{k,m},\ k=1,2,...,K \quad (1)$$

where T_m [K], X_m, and $a_{v,m}$ [cm^{-2}] are the local temperature, absorbing gas concentration, and absorbance density of $A_{v,k}$ in the mth grid, respectively [6]. P [atm] is the local pressure assumed to be 1. $L_{k,m}$ [cm] is the chord length of the kth laser beam passing through the mth grid. K is the total number of laser beams. $S_v(T)$ [cm^{-2}atm^{-1}] is the temperature-dependent line strength. In compact form,

$$\boldsymbol{A}_v=\boldsymbol{L}\boldsymbol{a}_v=P\boldsymbol{L}\left[\boldsymbol{X}\otimes S_v(\boldsymbol{T})\right] \quad (2)$$

$\boldsymbol{A}_v\in\mathbb{R}^{K\times1}$ is the path integrated absorbance vector. $\boldsymbol{T}\in\mathbb{R}^{M\times1}$, $\boldsymbol{X}\in\mathbb{R}^{M\times1}$, and $\boldsymbol{a}_v\in\mathbb{R}^{M\times1}$ are the temperature, gas concentration, and absorbance density vectors, respectively. $\boldsymbol{L}\in\mathbb{R}^{K\times M}$ is the chord length matrix in which the elements are $\{L_{k,m}: k=1,2,...,K, m=1,2,...,M\}$. $\otimes$ denotes element-wise multiplication. $S_v(\cdot)$ performs element-wise computation. In this work, temperature imaging, i.e., retrieval of $\boldsymbol{T}$, is exampled to demonstrate the proposed SpaProNet, since the temperature distribution is the most straightforward indication of thermal condition of the reaction, the combustion efficiency, and the formation of life-threatening pollutants, e.g., NO_x, CO, and soot [23].

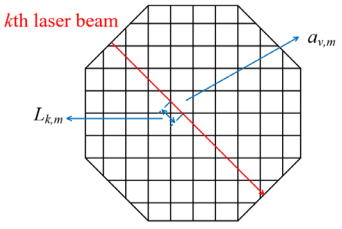

Fig. 1. A line-of-sight TDLAST measurement in the uniformly discretized sensing region.

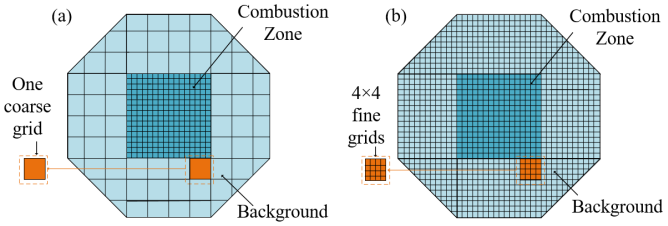

Fig. 2. LPGP discretization with J=4. (a) C-BG discretization and (b) F-BG discretization.

III. Local-Prior-Global-Progressive Discretization

To highlight temperature imaging in the combustion zone (CZ), and progressively and effectively allocate computational force for the background (BG), the LPGP discretization is designed with the following two discretization schemes:

1) C-BG discretization – fine discretization of the CZ and coarse discretization of the BG. The CZ is discretized into M_{CZ} dense grids with size of $H_{CZ} \times W_{CZ}$, while the BG is discretized into $M_{C\text{-}BG}$ coarse grids with size of $H_{C\text{-}BG} \times W_{C\text{-}BG}$. Here, $H_{C\text{-}BG} > H_{CZ}$ and $W_{C\text{-}BG} > W_{CZ}$.

2) F-BG discretization – fine discretization of both the CZ and the BG. The CZ is discretized densely as 1), while each coarse grid in the BG of the C-BG discretization is further split into $J \times J$ fine grids. That is, the BG is discretized into $M_{F\text{-}BG} = M_{C\text{-}BG} \times J^2$ fine grids with size of $H_{F\text{-}BG} \times W_{F\text{-}BG} = (H_{C\text{-}BG} / J) \times (W_{C\text{-}BG} / J)$.

Fig. 2 demonstrates the LPGP discretization with (a) the C-BG discretization and (b) the F-BG discretization with $J = 4$. Each grid in the BG in Fig. 2 (a) is split into 4 × 4 grids in the BG in Fig. 2 (b).

With this LPGP discretization, $\boldsymbol{A}_v$ in (2) can be written as

$$\boldsymbol{A}_v = P\boldsymbol{L}^{CZ}\left[\boldsymbol{X}^{CZ} \otimes S_v(\boldsymbol{T}^{CZ})\right] + P\boldsymbol{L}^{C\text{-}BG}\left[\boldsymbol{X}^{C\text{-}BG} \otimes S_v(\boldsymbol{T}^{C\text{-}BG})\right] \quad (3)$$

for the C-BG discretization, and

$$\boldsymbol{A}_v = P\boldsymbol{L}^{CZ}\left[\boldsymbol{X}^{CZ} \otimes S_v(\boldsymbol{T}^{CZ})\right] + P\boldsymbol{L}^{F\text{-}BG}\left[\boldsymbol{X}^{F\text{-}BG} \otimes S_v(\boldsymbol{T}^{F\text{-}BG})\right] \quad (4)$$

for the F-BG discretization, respectively. Here, $\boldsymbol{T}^{CZ} \in \mathbb{R}^{M_{CZ}\times 1}$, $\boldsymbol{X}^{CZ} \in \mathbb{R}^{M_{CZ}\times 1}$, and $\boldsymbol{L}^{CZ} \in \mathbb{R}^{K\times M_{CZ}}$ denote the temperature vector, the gas concentration vector, and the chord length matrix of the CZ. $\boldsymbol{T}^{C\text{-}BG} \in \mathbb{R}^{M_{C\text{-}BG}\times 1}$ ($\boldsymbol{T}^{F\text{-}BG} \in \mathbb{R}^{M_{F\text{-}BG}\times 1}$), $\boldsymbol{X}^{C\text{-}BG} \in \mathbb{R}^{M_{C\text{-}BG}\times 1}$ ($\boldsymbol{X}^{F\text{-}BG} \in \mathbb{R}^{M_{F\text{-}BG}\times 1}$), and $\boldsymbol{L}^{C\text{-}BG} \in \mathbb{R}^{K\times M_{C\text{-}BG}}$ ($\boldsymbol{L}^{F\text{-}BG} \in \mathbb{R}^{K\times M_{F\text{-}BG}}$) denote the temperature vector, the gas concentration vector, and the chord length matrix of the BG of C-BG (F-BG) discretization. The inverse problem of the spatially progressive TDLAST discussed in this work is to reconstruct CZ-prioritized temperature vector $\boldsymbol{T}^{C} = \begin{bmatrix}\boldsymbol{T}^{CZ}\\ \boldsymbol{T}^{C\text{-}BG}\end{bmatrix} \in \mathbb{R}^{(M_{CZ}+M_{C\text{-}BG})\times 1}$ and globally prioritized temperature vector $\boldsymbol{T}^{F} = \begin{bmatrix}\boldsymbol{T}^{CZ}\\ \boldsymbol{T}^{F\text{-}BG}\end{bmatrix} \in \mathbb{R}^{(M_{CZ}+M_{F\text{-}BG})\times 1}$ with different computational costs from $\boldsymbol{A}_{v_1} \in \mathbb{R}^{K\times 1}$ and $\boldsymbol{A}_{v_2} \in \mathbb{R}^{K\times 1}$ measured at two pre-selected transitions, v_1 and v_2.

IV. Network Establishment

A. System Setup

The multiple-output neural network, named as SpaProNet, is developed to realize spatially progressive temperature imaging for the TDLAST sensors with K laser beams. In this work, a lab-scale 32-beam TDLAST sensor is designed to validate the SpaProNet. The arrangement of the 32 laser beams is shown in Fig. 3. As demonstrated in [24], four-angle projection, that is 45° angular spacing between projections, is very cost-effective for maximizing the spatial resolution of TDLAST with limited number of laser beams. We denote the numbers of projection angles, the equispaced parallel beams at each angle, and the selected transitions as R, Q, and V, respectively. Here, $R = 4$, $Q = 8$, $V = 2$, and $K = R \times Q = 32$. The spacing between neighboring parallel beams within each projection is 18 mm. The sensing region is octagonal, with its side length of 144 mm. Water vapor (H_2O), a major product of hydrocarbon combustion, is selected as the target absorbing gas. Two H_2O transitions at $v_1 = 7185.60$ cm^{-1} and $v_2 = 7444.36$ cm^{-1} are chosen for experimental study given their good temperature sensitivity over 300-1200 K [25]. With this 32-beam TDLAST sensor, measurements $\boldsymbol{A}_{v_1} \in \mathbb{R}^{32\times 1}$ and $\boldsymbol{A}_{v_2} \in \mathbb{R}^{32\times 1}$ are obtained at v_1 and v_2, respectively.

The local combustion happens in the central square area with the side length of 144 mm. According to the LPGP discretization, the CZ is discretized into 40 × 40 dense grids. $M_{CZ} = 1600$ and $H_{CZ} \times W_{CZ} = 3.6$ mm × 3.6 mm. For the C-BG discretization, the BG is discretized into 364 coarse grids. $M_{C\text{-}BG} = 364$ and $H_{C\text{-}BG} \times W_{C\text{-}BG} = 14.4$ mm × 14.4 mm. For the F-BG discretization, the BG is discretized into 5824 fine grids. $J = 4$, $M_{F\text{-}BG} = 5824$, and $H_{F\text{-}BG} \times W_{F\text{-}BG} = 3.6$ mm × 3.6 mm.

B. Network Implementation

Taking $\boldsymbol{A}_{v_1}^{reshape} \in \mathbb{R}^{Q\times R}$ and $\boldsymbol{A}_{v_2}^{reshape} \in \mathbb{R}^{Q\times R}$, reshaped from $\boldsymbol{A}_{v_1} \in \mathbb{R}^{K\times 1}$ and $\boldsymbol{A}_{v_2} \in \mathbb{R}^{K\times 1}$, as inputs, the SpaProNet consists of two stages, as shown in Fig. 4, i.e., a locally prioritized reconstruction stage and a globally prioritized reconstruction stage, which output temperature vectors $\hat{\boldsymbol{T}}^{C}$ and $\hat{\boldsymbol{T}}^{F}$ with the BG coarsely and finely reconstructed, respectively.

1) Locally prioritized reconstruction stage

A CNN-based sub-network is constructed in this stage. As shown in Fig. 4, it consists of three convolutional layers i.e., Conv1~Conv3, one Squeeze-and-Excitation (SE) block [26], and four fully-connected layers, i.e., FC1~FC4. Conv1~Conv3 model multi-scale spatial dependencies in LoS measurements $[\boldsymbol{A}_{v_1}^{reshape}; \boldsymbol{A}_{v_2}^{reshape}] \in \mathbb{R}^{Q\times R\times 2}$ and output convolutional features $\boldsymbol{O}_{Conv1}$, $\boldsymbol{O}_{Conv2}$, and $\boldsymbol{O}_{Conv3}$, respectively. The SE block models the inter-dependencies among the channels of $\boldsymbol{O}_{Conv3}$. Different from existing data-driven tomographic algorithms in [15, 16, 18, 19], multi-scale spatial and cross-frequency features extracted by convolutional layers are combined here and mapped with

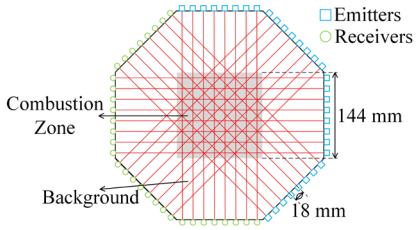

Fig. 3. Beam arrangement of the 32-beam TDLAST sensor.

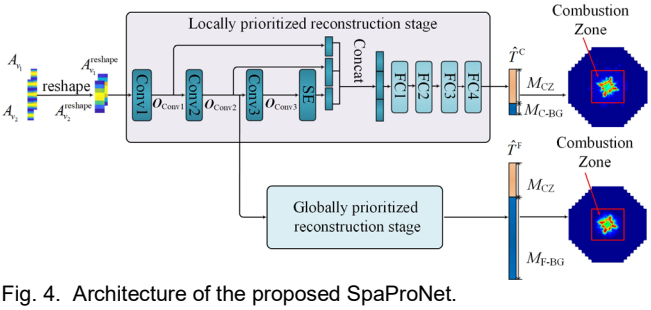

Fig. 4. Architecture of the proposed SpaProNet.

FC1~FC4 to retrieve temperature vector $\hat{\boldsymbol{T}}^{\mathrm{C}}$ of C-BG discretization. The forward propagation can be described as

$$\hat{\boldsymbol{T}}^{\mathrm{C}}=\mathrm{FC}_4\left(\mathrm{FC}_3\left(\mathrm{FC}_2\left(\mathrm{FC}_1\left(\mathrm{Concat}\left(\boldsymbol{O}_{\mathrm{Conv1}},\boldsymbol{O}_{\mathrm{Conv2}},\mathrm{SE}\left(\boldsymbol{O}_{\mathrm{Conv3}}\right)\right)\right)\right)\right)\right) \tag{5}$$

where SE(·), Concat(·), and FC$_i$(·) represent the operations of SE, concatenation, and FCi for $i\in\{1,2,3,4\}$, respectively.

The output of this stage is the temperature vector $\hat{\boldsymbol{T}}^{\mathrm{C}}$ with the CZ finely reconstructed and the BG coarsely reconstructed.

2) Globally prioritized reconstruction stage

The Transformer architecture is notable for its use of attention mechanisms [27] to model long-range dependencies in the data. Its success in the natural language processing domain has attracted researchers to investigate its applications to computer vision [28, 29]. In this work, Vision Transformer (ViT) [29] is introduced into the globally prioritized reconstruction stage of the SpaProNet to reconstruct the 2-D temperature distribution with fine spatial resolution for both the CZ and the BG.

As shown in Fig. 5, this stage consists of a patch partition and embedding layer, a two-branch Transformer Encoder, and a Multi-Layer Perceptron (MLP) layer. $\boldsymbol{O}_{\mathrm{Conv2}}$, featuring spatial and cross-frequency correlations of the LoS measurements, are organized into a sequence of expanded patches via the patch partition and embedding layer. The short-range and long-range dependencies among the patches are subsequently modeled by the two-branch Transformer Encoder, and finally mapped to the temperature vector in F-BG discretization by the MLP layer.

In detail, the input $\boldsymbol{O}_{\mathrm{Conv2}}\in\mathbb{R}^{H_{O2}\times W_{O2}\times C_{O2}}$ is reshaped into a sequence of flattened patches $\boldsymbol{x}^0=(\boldsymbol{x}_1^0;\boldsymbol{x}_2^0;\ldots;\boldsymbol{x}_{N_{\mathrm{patch}}}^0)\in\mathbb{R}^{N_{\mathrm{patch}}\times(H_pW_pC_{O2})}$, where $H_p\times W_p$ is the patch size and $N_{\mathrm{patch}}=(H_{O2}\times W_{O2})/(H_P\times W_P)$ is the number of patches. Then, each element $\boldsymbol{x}_i^0\in\mathbb{R}^{1\times(H_pW_pC_{O2})}$ of $\boldsymbol{x}^0$, $i\in\{1,2,\ldots,N_{\mathrm{patch}}\}$, is taken as a "token" and mapped to patch embedding $\boldsymbol{x}_i^0\boldsymbol{W}_L\in\mathbb{R}^{1\times D}$ with a linear projection matrix $\boldsymbol{W}_L\in\mathbb{R}^{(H_pW_pC_{O2})\times D}$, where D is the constant vector dimension throughout all layers of the two-branch Transformer Encoder. A embedding $\boldsymbol{z}_0^0\in\mathbb{R}^{1\times D}$ is prepended to the sequence of embedded patches, whose state at the output of the two-branch Transformer Encoder serves as the input of the MLP layer. After adding position embedding $\boldsymbol{W}_{\mathrm{pos}}\in\mathbb{R}^{(N_{\mathrm{patch}}+1)\times D}$, the output $\boldsymbol{Z}_0\in\mathbb{R}^{(N_{\mathrm{patch}}+1)\times D}$ of the patch partition and embedding layer can be descried as

$$\boldsymbol{Z}_0=\left[\boldsymbol{z}_0^0;\boldsymbol{x}_1^0\boldsymbol{W}_L;\boldsymbol{x}_2^0\boldsymbol{W}_L;\ldots;\boldsymbol{x}_{N_{\mathrm{patch}}}^0\boldsymbol{W}_L\right]+\boldsymbol{W}_{\mathrm{pos}} \tag{6}$$

The two-branch Transformer Encoder is composed of a stack of N_{layer} layers, which are of identical structure but use different parameters from layer to layer. In the lth layer, $l\in\{1,2,\ldots,N_{\mathrm{layer}}\}$, $\boldsymbol{Z}_{l-1}\in\mathbb{R}^{(N_{\mathrm{patch}}+1)\times D}$ and $\boldsymbol{Z}_l\in\mathbb{R}^{(N_{\mathrm{patch}}+1)\times D}$ denote the input and output, respectively. As shown in the dashed box in Fig. 5, the lth layer contains two branches. One branch models the long-range dependencies in $\boldsymbol{Z}_{l-1}$ with a Multi-headed Self Attention (MSA) sub-layer and a Feed-Forward Network (FFN) sub-layer. The other branch models the short-range dependencies in $\boldsymbol{Z}_{l-1}$ with convolutional layers. Operations performed in the MSA sub-layer, the FFN sub-layer, and the convolutional branch are described as below.

(i) MSA sub-layer

A total of N_{SA} self-attention operations $\mathrm{SA}_h(\cdot)$, $h\in\{1,2,\ldots,N_{\mathrm{SA}}\}$, called "heads", are run on normalized input $\bar{\boldsymbol{Z}}_{l-1}=\mathrm{LN}(\boldsymbol{Z}_{l-1})$ in parallel, where LN(·) denotes the layer normalization. Their concatenated outputs are linearly projected by $\boldsymbol{W}_{\mathrm{MSA}}\in\mathbb{R}^{N_{\mathrm{SA}}D_{\mathrm{head}}\times D}$, in which D_{head} is the dimension of each head. The output of this sub-layer $\boldsymbol{Z}_l'\in\mathbb{R}^{(N_{\mathrm{patch}}+1)\times D}$ is

$$\boldsymbol{Z}_l'=\boldsymbol{Z}_{l-1}+\mathrm{Concat}\left(\mathrm{SA}_1(\bar{\boldsymbol{Z}}_{l-1}),\ldots,\mathrm{SA}_{N_{\mathrm{SA}}}(\bar{\boldsymbol{Z}}_{l-1})\right)\boldsymbol{W}_{\mathrm{MSA}} \tag{7}$$

The self-attention operation of the hth head $\mathrm{SA}_h(\bar{\boldsymbol{Z}}_{l-1})$ is

$$\mathrm{SA}_h(\bar{\boldsymbol{Z}}_{l-1})=\mathrm{softmax}\left(\boldsymbol{Q}_h\boldsymbol{K}_h^{\mathrm{T}}/\sqrt{D_{\mathrm{head}}}\right)\boldsymbol{V}_h \tag{8}$$

$$[\boldsymbol{Q}_h,\boldsymbol{K}_h,\boldsymbol{V}_h]=\bar{\boldsymbol{Z}}_{l-1}\boldsymbol{U}_h \tag{9}$$

where $\boldsymbol{U}_h\in\mathbb{R}^{D\times 3D_{\mathrm{head}}}$ is the projection matrix of the hth head. In this work, D_{head} is set as D/N_{SA}.

(ii) FFN sub-layer

This sub-layer consists of two linear transforms with nonlinearity in between, which are applied to each row in the normalized input $\bar{\boldsymbol{Z}}_l'=\mathrm{LN}(\boldsymbol{Z}_l')$ separately and identically. The output $\boldsymbol{Z}_l''\in\mathbb{R}^{(N_{\mathrm{patch}}+1)\times D}$ of this sub-layer is

$$\boldsymbol{Z}_l''=\boldsymbol{Z}_l'+\left(\mathrm{GELU}\left(\bar{\boldsymbol{Z}}_l'\boldsymbol{W}_1^{\mathrm{FFN}}+\boldsymbol{b}_1^{\mathrm{FFN}}\right)\boldsymbol{W}_2^{\mathrm{FFN}}+\boldsymbol{b}_2^{\mathrm{FFN}}\right) \tag{10}$$

Here, $\boldsymbol{W}_1^{\mathrm{FFN}}\in\mathbb{R}^{D\times n_{\mathrm{FFN}}}$ ($\boldsymbol{W}_2^{\mathrm{FFN}}\in\mathbb{R}^{n_{\mathrm{FFN}}\times D}$) and $\boldsymbol{b}_1^{\mathrm{FFN}}\in\mathbb{R}^{1\times n_{\mathrm{FFN}}}$ ($\boldsymbol{b}_2^{\mathrm{FFN}}\in\mathbb{R}^{1\times D}$) are the weight matrix and the bias vector of the first (second) linear transform, respectively. GELU(·) realizes the nonlinearity between the two linear transforms.

(iii) Convolutional branch

This branch models the short-range dependencies in $\boldsymbol{Z}_{l-1}$ with convolutional layers. In this work, one convolutional layer is

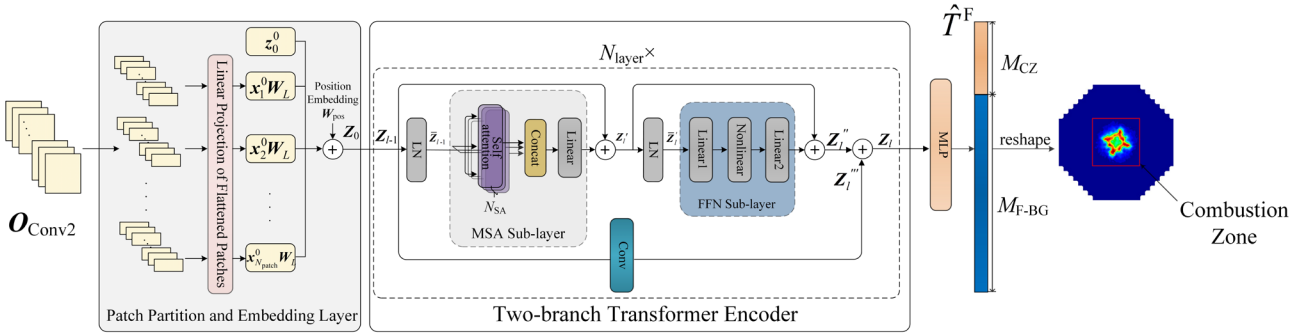

Fig. 5. Detailed architecture of the globally prioritized reconstruction stage.

exampled, i.e., the output of this branch is $\boldsymbol{Z}_l'''$ =Conv($\boldsymbol{Z}_{l\text{-}1}$) $\in \mathbb{R}^{(N_{\text{patch}}+1)\times D}$. The output $\boldsymbol{Z}_l$ of the lth layer of the two-branch Transformer Encoder is $\boldsymbol{Z}_l'' + \boldsymbol{Z}_l'''$.

With the above operations of N_{layer} layers, the output of the two-branch Transformer Encoder is $\boldsymbol{Z}_{N_{\text{layer}}} = [\boldsymbol{z}_0^{N_{\text{layer}}}; \boldsymbol{z}_1^{N_{\text{layer}}};...; \boldsymbol{z}_{N_{\text{patch}}}^{N_{\text{layer}}}]$. Its first element $\boldsymbol{z}_0^{N_{\text{layer}}} \in \mathbb{R}^{1\times D}$ is the input of the MLP layer, which consists of only one linear transform. The forward propagation of the MLP layer can be formulated as

$$\left(\hat{\boldsymbol{T}}^{\text{F}}\right)^{\text{T}} = \boldsymbol{z}_0^{N_{\text{layer}}}\boldsymbol{W}_{\text{MLP}} + \boldsymbol{b}_{\text{MLP}} \tag{11}$$

where $\boldsymbol{W}_{\text{MLP}} \in \mathbb{R}^{D\times n_{\text{MLP}}}$ and $\boldsymbol{b}_{\text{MLP}} \in \mathbb{R}^{1\times n_{\text{MLP}}}$ are the weight matrix and the bias vector of the MLP layer, respectively. n_{MLP} is set as $M_{\text{CZ}} + M_{\text{F-BG}}$. The output of this globally prioritized reconstruction stage is the temperature vector $\hat{\boldsymbol{T}}^{\text{F}}$ with both the CZ and BG finely retrieved.

V. Network Training and Testing

A. Network Training

To train the SpaProNet with hydrodynamics of the real reactive flows, the training dataset is constructed by cross-sectional distributions of temperature and H_2O concentration in a dynamic field that are generated by Large Eddy Simulation (LES) via Fire Dynamic Simulator (FDS) [30, 31]. With sufficient coverage of various simulation conditions, e.g., structures and dimensions of the burner, fuel/air flow rates, equivalent ratios, the LES is able to drive the SpaProNet with computational fluid dynamics (CFD) aided dataset. Instead of empirically penalizing the TDLAST inverse problem, the CFD-data driven SpaProNet performs hydrodynamics-informed learning and thus enabling good generalizability and applicability for real-world combustion processes.

In the simulation, a three-dimensional open-boundary domain, filled with air, is established. The reactive flow field is generated by a circular burner located at the bottom of the domain. The cross section of the domain is 347.6 mm × 347.6 mm, and discretized into high-resolution grids of 1.8 mm × 1.8 mm. Cross-sectional distributions of temperature and H_2O concentration over these high-resolution grids are generated. The synthetic path integrated absorbances $\boldsymbol{A}_{v_1} \in \mathbb{R}^{32\times 1}$ and $\boldsymbol{A}_{v_2} \in \mathbb{R}^{32\times 1}$ are generated using the highly-resolved gas parameters to a) guarantee a most accurate forward problem of TDLAST and b) incorporate realistic model errors in the data. Propane is chosen as the fuel. Eight different combustion processes are simulated by varying the diameter of the burner in range of {60 mm, 80 mm, 100 mm, 120 mm}. For each diameter, two different mass fractions of the propane, i.e., 0.2 kg/m^2/s and 0.1 kg/m^2/s, are introduced to cover high and low fuel flows, respectively. At 20 mm above the burner outlet, 150 consecutive frames of cross-sectional images of temperature and H_2O concentration are recorded at an interval of 0.1 s for each burning process. To expand diversity of the simulative dataset, these images are rotated by 9 angles with an angular spacing of 36°.

The dataset is generated according to the beam arrangement shown in Fig. 3. An individual sample is denoted as $((\boldsymbol{A}_{v_1}, \boldsymbol{A}_{v_2}), \boldsymbol{T}^{\text{C}}, \boldsymbol{T}^{\text{F}})$, where $\boldsymbol{A}_{v_1} \in \mathbb{R}^{32\times 1}$ and $\boldsymbol{A}_{v_2} \in \mathbb{R}^{32\times 1}$ are path integrated absorbances calculated over high-resolution grids according to (2). The LPGP discretization is applied on the simulated sensing region with the same settings as that for the lab-scale 32-beam TDLAST sensor described in Section IV A. $\boldsymbol{T}^{\text{C}} \in \mathbb{R}^{1964\times 1}$ and $\boldsymbol{T}^{\text{F}} \in \mathbb{R}^{7424\times 1}$ are temperature vectors of the C-BG and F-BG discretizations, respectively. Seven out of the eight simulated burning processes are selected to generate training data. To verify the generalization of the proposed network, sample no. 1 to sample no. 135 generated in each of the 7 selected burning process, i.e., 90% of the samples in sequence, are used as the training samples. The last 10% of the samples in sequence are used as the validation samples. To examine the performance of the trained network on reconstruction of unknown temperature distributions, the test is carried out by reconstruction of the one remaining burning process, in which the temperature distributions are independent of any of those in the previously selected 7 burning processes. 500 samples are generated in this burning process for test. Thus, the sizes of training set, validation set, and test set are N_{train} = 9,450, N_{valid} = 1,050, and N_{test} = 500, respectively.

The proposed SpaProNet is trained with Algorithm 1 over the noise-free training set. Hyper-parameters of the SpaProNet in the simulation are shown in Table I. Leaky ReLu is selected as the activation function for all convolutional layers. In Algorithm 1, $\boldsymbol{\Theta}_{\text{L}}^i$, $\boldsymbol{\Theta}_{\text{G}}^i$, and $\boldsymbol{\Theta}^i = \boldsymbol{\Theta}_{\text{L}}^i \cup \boldsymbol{\Theta}_{\text{G}}^i$ denote parameters sets updated in the ith iteration for the locally prioritized reconstruction stage, the globally prioritized reconstruction stage, and the whole network of SpaProNet, respectively. $L(\boldsymbol{T}, \hat{\boldsymbol{T}} \mid \boldsymbol{\Theta})$ calculates the

TABLE I Hyper-parameters of the SpaProNet

Locally prioritized reconstruction stage					**Globally prioritized reconstruction stage**						
	Input dim.	Weight matrix size	Stride	Output dim.		$H_{O2}\times W_{O2}\times C_{O2}$	$H_P\times W_P$	N_{SA}	D	D_{head}	n_{FFN}
Conv1	8×4×2	2×2	(1,1)	7×3×8	**Transformer**	6×2×16	1×2	4	64	16	1024
Conv2	7×3×8	2×2	(1,1)	6×2×16		Input dim.	Weight matrix size		Stride	n_{MLP}	Output dim.
Conv3	6×2×16	2×2	(1,1)	5×1×32	**Conv**	6×2×16	3×3		(1,1)	-	6×2×16
FC1	520	520×520	-	520							
FC2	520	1024×520	-	1024	**MLP**	64	7424×64		-	7424	7424
FC3	1024	1024×1024	-	1024							
FC4	1024	1964×1024	-	1964							

Mean Square Error (MSE) loss between the true $\boldsymbol{T}$ and the $\hat{\boldsymbol{T}}$ reconstructed under parameters set $\boldsymbol{\Theta}$

$$L(\boldsymbol{T},\hat{\boldsymbol{T}}\,|\,\boldsymbol{\Theta})=\left\|\boldsymbol{T}-\hat{\boldsymbol{T}}\right\|_2^2\Big/\left|\boldsymbol{T}\right| \tag{12}$$

where $|\boldsymbol{T}|$ is the length of vector $\boldsymbol{T}$. Batch size B, number of epochs E, and learning rate α are set as 64, 100, and 0.001, respectively. Adam optimizer is employed as Optimizer(·).

To the best of the authors' knowledge, none existing data-driven tomographic algorithms can reconstruct the two different objects, i.e., high-accuracy combustion zone and finely-resolved sensing region, by training a single network. To examine the performance of the proposed SpaProNet, it is compared with the other three state-of-the-art data-driven algorithms for TDLAST and computer vision. All these three networks are adapted for our 32-beam TDLAST sensor, where the distribution of temperature is reconstructed from $\boldsymbol{A}_{v_1}\in\mathbb{R}^{32\times1}$ and $\boldsymbol{A}_{v_2}\in\mathbb{R}^{32\times1}$. Moreover, each network is adapted into two forms. One form, named with suffix "-LP", reconstructs temperature vector $\hat{\boldsymbol{T}}^{\mathrm{C}}\in\mathbb{R}^{1964\times1}$ of the C-BG discretization, while the other form, named with suffix "-GP", reconstructs temperature vector $\hat{\boldsymbol{T}}^{\mathrm{F}}\in\mathbb{R}^{7424\times1}$ of the F-BG discretization.

Algorithm 1 The training algorithm for SpaProNet

Input: training set $\{((\boldsymbol{A}_{v_1,\tau},\boldsymbol{A}_{v_2,\tau}),\boldsymbol{T}_\tau^{\mathrm{C}},\boldsymbol{T}_\tau^{\mathrm{F}}):\tau=1,2,...,N_{\mathrm{train}}\}$, batch size B, number of epochs E, and learning rate α.

Initialize: $N_{\mathrm{batch}}\leftarrow\mathrm{floor}(N_{\mathrm{train}}/B)$; $i\leftarrow0$; Parameters in sets $\boldsymbol{\Theta}_{\mathrm{L}}^0$ and $\boldsymbol{\Theta}_{\mathrm{G}}^0$ are randomly initialized; $\boldsymbol{\Theta}^0\leftarrow\boldsymbol{\Theta}_{\mathrm{L}}^0\cup\boldsymbol{\Theta}_{\mathrm{G}}^0$

Iterations:

For $t=1$ to E **do**

Training samples are randomly divided into N_{batch} batches;

For $b=1$ to N_{batch} **do**

$i\leftarrow i+1$

Get the bth batch $\{((\boldsymbol{A}_{v_1,s},\boldsymbol{A}_{v_2,s}),\boldsymbol{T}_s^{\mathrm{C}},\boldsymbol{T}_s^{\mathrm{F}}):s=1,2,...,B\}$;

For $s=1$ to B **do**

Input $\boldsymbol{A}_{v_1,s}$ and $\boldsymbol{A}_{v_2,s}$, propagate forward through SpaProNet, output locally prioritized reconstruction $\hat{\boldsymbol{T}}_s^{\mathrm{C}}$ and globally prioritized reconstruction $\hat{\boldsymbol{T}}_s^{\mathrm{F}}$;

Calculate $L_s^{\text{sample-L}}$ of the sth sample in the bth batch as $L_s^{\text{sample-L}}\leftarrow L(\boldsymbol{T}_s^{\mathrm{C}},\hat{\boldsymbol{T}}_s^{\mathrm{C}}\,|\,\boldsymbol{\Theta}_{\mathrm{L}}^{i-1})$

Calculate $L_s^{\text{sample-G}}$ of the sth sample in the bth batch as $L_s^{\text{sample-G}}\leftarrow L(\boldsymbol{T}_s^{\mathrm{F}},\hat{\boldsymbol{T}}_s^{\mathrm{F}}\,|\,\boldsymbol{\Theta}_{\mathrm{G}}^{i-1})$

End for

Calculate $L_b^{\text{batch-L}}$ of the bth batch as $L_b^{\text{batch-L}}\leftarrow\frac{1}{B}\sum_{s=1}^{B}L_s^{\text{sample-L}}$

Calculate $L_b^{\text{batch-G}}$ of the bth batch as $L_b^{\text{batch-G}}\leftarrow\frac{1}{B}\sum_{s=1}^{B}L_s^{\text{sample-G}}$

Update $\boldsymbol{\Theta}_{\mathrm{L}}^i$ by back propagation as $\boldsymbol{\Theta}_{\mathrm{L}}^i\leftarrow\mathrm{Optimizer}(\boldsymbol{\Theta}_{\mathrm{L}}^{i-1}\,|\,L_b^{\text{batch-L}},\alpha)$

Update $\boldsymbol{\Theta}_{\mathrm{G}}^i$ by back propagation as $\boldsymbol{\Theta}_{\mathrm{G}}^i\leftarrow\mathrm{Optimizer}(\boldsymbol{\Theta}_{\mathrm{G}}^{i-1}\,|\,L_b^{\text{batch-G}},\alpha)$

$\boldsymbol{\Theta}^i\leftarrow\boldsymbol{\Theta}_{\mathrm{L}}^i\cup\boldsymbol{\Theta}_{\mathrm{G}}^i$

End for

End for

Output: parameters set $\boldsymbol{\Theta}^i$

1) Huang's CNN (H-CNN). Here, the pioneering CNN-based temperature imaging network established in [15] is adapted into two separate networks, i.e., H-CNN-LP and H-CNN-GP, to reconstruct temperature vectors $\hat{\boldsymbol{T}}^{\mathrm{C}}$ and $\hat{\boldsymbol{T}}^{\mathrm{F}}$, respectively. Fully-connected layers are added to H-CNN-LP and H-CNN-GP to make the numbers of trainable parameters close to those of SpaProNet-LP and SpaProNet-GP, respectively.

2) QHT-LSTM [18]. This is the first work of developing progressive data-driven tomographic algorithm for TDLAST. However, the two temperature images reconstructed by QHT-LSTM are of the same spatial resolutions. Here, QHT-LSTM is adapted into two separate networks, i.e., QHT-LSTM-LP and QHT-LSTM-GP, to finally reconstruct $\hat{\boldsymbol{T}}^{\mathrm{C}}$ and $\hat{\boldsymbol{T}}^{\mathrm{F}}$, respectively.

3) SwinT-T [19]. Swin Transformer is a new vision Transformer that serves as a general-purpose backbone for computer vision [32]. SwinT-T is a Swin Transformer based network recently established for TDLAST temperature imaging. It computes MSA in regularly partitioned windows and shifted windows alternatively to introduce cross-window connections while maintaining the efficient computation of local non-overlapped windows. Here, SwinT-T is adapted into two separate networks, i.e., SwinT-T-LP and SwinT-T-GP, to reconstruct $\hat{\boldsymbol{T}}^{\mathrm{C}}$ and $\hat{\boldsymbol{T}}^{\mathrm{F}}$, respectively.

The numbers of trainable parameters of these networks are stated in Table II. All networks are trained and tested on the same dataset with Pytorch framework on a computer with Intel i5-7300h CPU, NVIDA GeForce GTX 1050 Ti GPU, and 8G memory. These computing resources can be equipped on the host PC in the existing industrial applications of TDLAST systems, such as diagnostics of aero-engine exhaust [22] and wind tunnels [33]. Moreover, the proposed network can be potentially deployed on System-on-a-Chip (SoC), such as a Field Programmable Gate Array (FPGA) [34, 35], to accelerate the image reconstruction.

B. Test Results

The data acquisition process is simulated by adding physically meaningful noise [36, 37], i.e., frequency-dependent noise and frequency-independent noise, of different levels on the laser transmission. The frequency-dependent noise mainly contains pink noise (1/f noise), e.g., laser and detector excess noise, and low-frequency environmental noise generally caused by flow-induced beam steering. The frequency-independent noise, known as white noise, is dominated by the thermal noise from the detector, signal amplification, and digitization circuits. In the simulation, the Signal to Noise Ratio (SNR) depicts the level of the physically meaningful noise on the digitized laser transmission signal. Then, path integrated absorbances $\boldsymbol{A}_v$ are extracted from the noise-contaminated laser transmission.

Tests are carried out in a practical range of 12.5 dB SNRs, from 35 dB to 47.5 dB with an interval of 2.5 dB. Optimally

TABLE II NUMBERS OF TRAINABLE PARAMETERS OF SPAPRONET AND THE ADAPTED EXISTING NETWORKS

-LP	H-CNN	QHT-LSTM	SwinT-T	SpaProNet
Parameters	3.88 M	6.32 M	4.36 M	3.87 M
-GP	H-CNN	QHT-LSTM	SwinT-T	SpaProNet
Parameters	5.26 M	17.79 M	11.36 M	5.54 M

trained H-CNN-LP/-GP, QHT-LSTM-LP/-GP, SwinT-T-LP /-GP, and SpaProNet are implemented individually on the test set at various SNRs. In the following, visual and quantitative metric comparisons are carried out among H-CNN-LP, QHT-LSTM-LP, SwinT-T-LP, and SpaProNet-LP for locally prioritized temperature reconstruction, and among H-CNN-GP, QHT-LSTM-GP, SwinT-T-GP, and SpaProNet-GP for globally prioritized temperature reconstruction.

Firstly, reconstructed temperature images are visually inspected. Fig. 6 (a) shows a temperature phantom obtained from the FDS. Figs. 6 (b-i) show the reconstructions at the SNR of 35 dB using H-CNN-LP, H-CNN-GP, QHT-LSTM-LP, QHT-LSTM-GP, SwinT-T-LP, SwinT-T-GP, the proposed SpaProNet-LP and SpaProNet-GP, respectively. It can be seen that all the reconstructions are capable of indicating the temperature profile with correct position of the flame. The visual comparison is carried out on the combustion zone and the global image, respectively. Two results can be drawn here:

1) SpaProNet-LP outperforms other networks for the reconstruction of the combustion zone.

2) SpaProNet-GP gives better-quality image for the entire sensing region than other networks.

Then, the reconstruction fidelity is compared under different SNRs with quantitative evaluation. Relative Reconstruction Error (RRE) e is defined to quantify the pixel-wised reconstruction error as

$$e = \frac{1}{|\boldsymbol{T}|}\sum_{j=1}^{|\boldsymbol{T}|}\frac{\left|\hat{T}_j - T_j\right|}{T_j} \tag{13}$$

where T_j and $\hat{T}_j$ are the jth elements in the true temperature vector $\boldsymbol{T}$ and the reconstructed temperature vector $\hat{\boldsymbol{T}}$ over the high-resolution ground-truth grids of 1.8 mm × 1.8 mm, respectively. When calculating RRE for the CZ and the entire sensing region, $\hat{\boldsymbol{T}}^{\mathrm{CZ}}$ and $\hat{\boldsymbol{T}}^{\mathrm{C}}$ ($\hat{\boldsymbol{T}}^{\mathrm{F}}$) are projected to the temperature vectors $\hat{\boldsymbol{T}} \in \mathbb{R}^{6400\times 1}$ and $\hat{\boldsymbol{T}} \in \mathbb{R}^{29696\times 1}$ over the high-resolution grids with uniform interpolation, respectively. To characterize the overall reconstruction fidelity of the network over the test set, RREs are averaged on $\{\boldsymbol{e}_\tau : \tau = 1, 2, \ldots, N_{\mathrm{test}}\}$ achieved for all test samples as

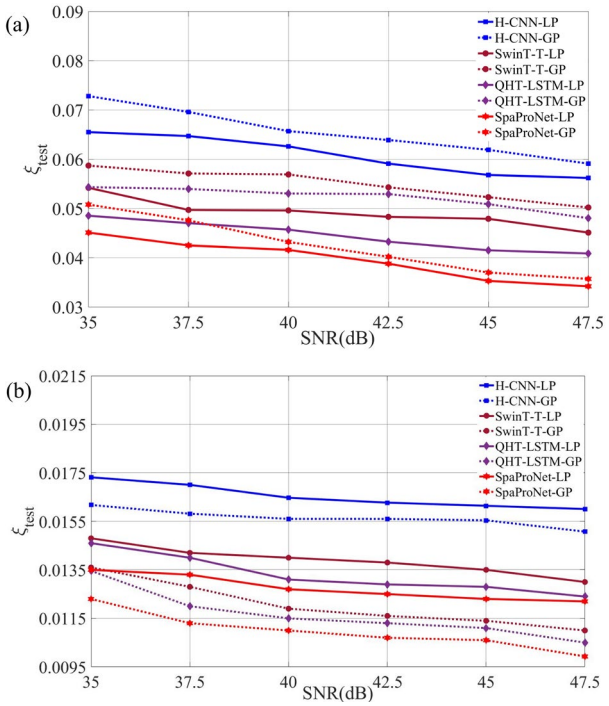

Fig. 7. ξ_{test} obtained for (a) the combustion zone and (b) the entire sensing region using the data-driven algorithms at given SNRs.

$$\xi_{\mathrm{test}} = \frac{1}{N_{\mathrm{test}}}\sum_{\tau=1}^{N_{\mathrm{test}}} e_\tau \tag{14}$$

Fig. 7 depicts ξ_{test} obtained by all the above-mentioned networks at different SNRs. Figs. 7 (a) and (b) show ξ_{test} of the CZ and the global image reconstructed by H-CNN-LP/-GP, QHT-LSTM-LP/-GP, SwinT-T-LP/-GP, and SpaProNet-LP/GP, respectively. As shown in Fig. 7 (a), at all the given SNRs, ξ_{test} of the CZ obtained by SpaProNet-LP is always lower than those obtained by the other networks. For example, in comparison with H-CNN-LP, SwinT-T-LP, and QHT-LSTM-LP, SpaProNet-LP suppresses ξ_{test} of the CZ by 31.14%, 16.78%, and 7.01% at the SNR of 35 dB, respectively. As shown in Fig.

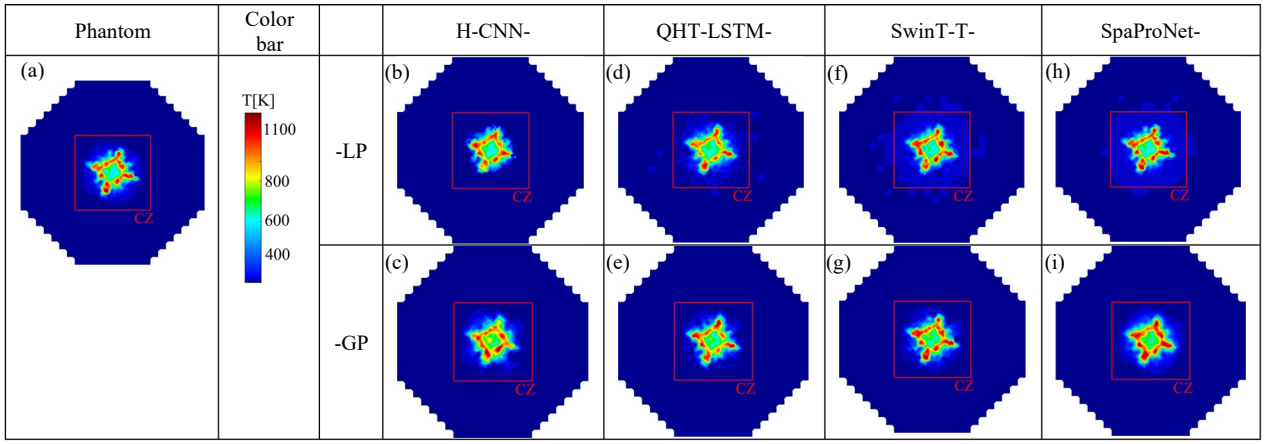

Fig. 6. Reconstruction of a simulated temperature phantom. (a) shows the true temperature distribution. (b-i) show temperature images reconstructed at the SNR of 35 dB using H-CNN-LP, H-CNN-GP, QHT-LSTM-LP, QHT-LSTM-GP, SwinT-T-LP, SwinT-T-GP, SpaProNet-LP, and SpaProNet-GP, respectively.

7 (b), ξ_{test} of the global image obtained by SpaProNet-GP is the lowest at the given SNRs. In comparison with H-CNN-GP, SwinT-T-GP, and QHT-LSTM-GP, SpaProNet-GP suppresses ξ_{test} of the global image by 21.96%, 8.78%, and 7.53% at the SNR of 35 dB, respectively.

Finally, training time for all the networks are compared. As shown in Table III, QHT-LSTM-LP/-GP, SwinT-T-LP/-GP, and SpaProNet take longer training time than H-CNN-LP/-GP. This is because of the more complex network structures established in QHT-LSTM, SwinT-T, and SpaProNet to achieve higher-fidelity performance than H-CNN. Once optimally trained, SpaProNet can realize both locally prioritized reconstruction and globally prioritized reconstruction. In contrast, H-CNN, QHT-LSTM, and SwinT-T must be trained twice to realize locally prioritized reconstruction and globally prioritized reconstruction individually.

VI. Experimental Validation

With the 32-beam TDLAST sensor built as described in Section IV. A, we carry out lab-scale experiments to further validate the performance of the proposed SpaProNet. More details of the optics and hardware electronics of the experimental system can be found in [9, 37].

In the sensing region, there is a propane-fueled burner located at the center shown in Fig. 8 (a). The fuels are released from the annular injectors, which is similar as the simulated scenarios in Section V. Since the LES results are convincing to qualitatively characterize of the target flames in terms of approximate temperature range, dimensions of the hot spot and fluctuation frequency, the proposed networks should be capable of imaging an independent burning process that shares quantitative similarities. Real measurement data, $\boldsymbol{A}_{v_1} \in \mathbb{R}^{32\times1}$ and $\boldsymbol{A}_{v_2} \in \mathbb{R}^{32\times1}$, are obtained from the 32-beam TDLAST sensor. The real measurement data are input to each optimally trained network. As shown in Figs. 8 (b-i), temperature distributions are finally reconstructed from H-CNN-LP, H-CNN-GP, QHT-LSTM-LP, QHT-LSTM-GP, SwinT-T-LP, SwinT-T-GP, SpaProNet-LP, and SpaProNet-GP, respectively.

In all the reconstructed images, the retrieved flame locations in the CZ agree well with that of the real one. However, the flames reconstructed by H-CNN-LP and H-CNN-GP shown in Figs. 8 (b) and (c) indicate obvious temperature discontinuity of the annular combustion in the real flame. As shown in Figs. 8 (d) and (e), the profile of the high-temperature zones in the CZ reconstructed by QHT-LSTM-LP disagrees with that reconstructed by QHT-LSTM-GP. Although the flames reconstructed by SwinT-T-LP and SwinT-T-GP shown in Figs. 8 (f) and (g) could reflect the annular combustion, discrepancy can be observed on the sizes of the reconstructed annular combustion. In contrast, good agreement is achieved by the temperature distributions reconstructed in the CZ by the SpaProNet-LP and the SpaProNet-GP shown in Figs. 8 (h) and (i). In addition, the image generated by the SpaProNet-GP has the most uniform temperature distribution in the region out of the high-temperature zones, outperforming the other methods with artefacts there.

Furthermore, quantitative comparison is performed between the temperature values extracted from the reconstructions and those measured by the thermocouple (TC). The TC measurements are carried out at the same height as the tomographic cross section. The TC is scanned radially from the center to the boundary of the flame, giving point-wised and time-averaged reference temperature values at the interval of 10 mm along the radial direction. Since the burner outlet is rotationally symmetric, the radial scans are repeated at different angles to reduce measurement uncertainties. These radial TC measured temperature values, as well as those reconstructed by each model, are averaged and plotted in Fig. 9. It can be seen the radial temperature values retrieved by both the SpaProNet-LP and SpaProNet-GP are the closest to the TC measurements in the two reconstruction stages, indicating their better accuracy than the other state-of-the-art data-driven algorithms.

TABLE III Comparison of Training Time for the Evaluated Networks

Network	H-CNN-LP	H-CNN-GP	QHT-LSTM-LP	QHT-LSTM-GP	SwinT-T-LP	SwinT-T-GP	SpaProNet
Training time [min]	1.75	2.99	4.85	6.15	7.99	12.22	7.07

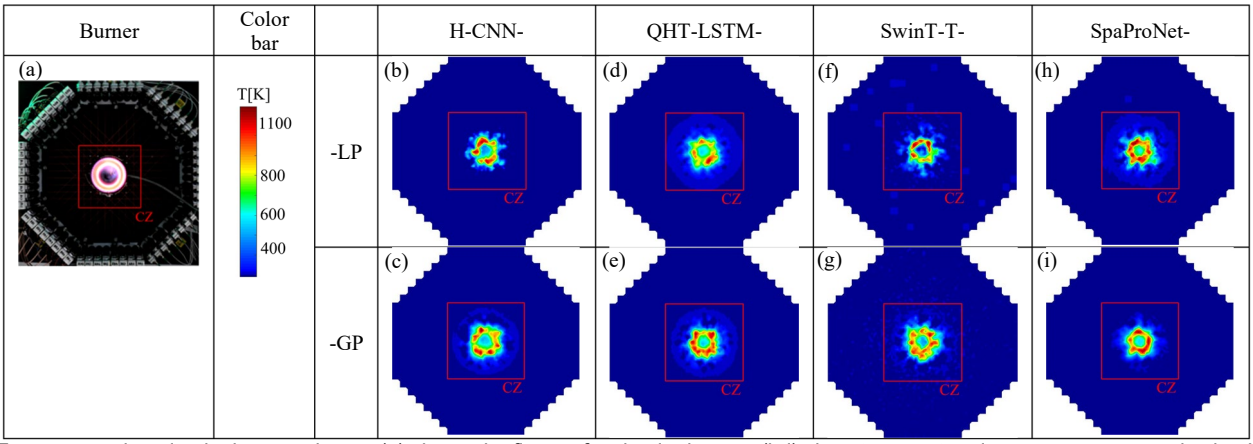

Fig. 8. Temperature imaging in the experiment. (a) shows the flame of a circular burner. (b-i) show temperature images reconstructed using H-CNN-LP, H-CNN-GP, QHT-LSTM-LP, QHT-LSTM-GP, SwinT-T-LP, SwinT-T-GP, SpaProNet-LP, and SpaProNet-GP, respectively.

Given annular fuel injectors on the burner surface, the flame, in principle, should generate annular hot regions when the tomographic cross section is located close to the burner surface, for example, the 20 mm height in the experiments in this work. The radial temperature distribution should be similar as the reconstructed ones with temperature at the flame center lower than that in the annular hot regions. When measuring such a temperature field using the TC, the TC bead is located at the center where the temperature is lower, while the TC wire neighboring the bead is located in a hotter region. As noted in [38], the heat conducted from the wire to the bead will result into a higher TC measured temperature than the true gas temperature. That is to say, the TC measured temperature at the flame center, i.e., x=0 in Fig. 9, should be corrected to give a lower temperature. This correction will give better agreement between the TC measurements and the reconstructions.

In the application of imaging the aero-engine exhaust using TDLAST [22], the CZ encloses the reactions in the plume, while the BG contains the information of heat radiation from the plume and plume-air interactions. When the CZ is of more interested, the SpaProNet-LP with the C-BG discretization scheme is suitable to highlight the reconstruction in the CZ with finely discretized meshes, and to consider the absorption in the BG and the integrity of the line-of-sight TDLAST formulation with coarsely discretized meshes. The SpaProNet-LP gives better accuracies in the CZ but at the sacrifice of the BG accuracies. When both the CZ and BG are of interested, the SpaProNet-GP with the F-BG discretization scheme can detail the entire sensing region with finely discretized meshes. Since the unknown parameters in more pixels need to be learned, the SpaProNet-GP balance the computational resources between the CZ and BG, and gives better accuracy of the entire sensing region than the SpaProNet-LP.

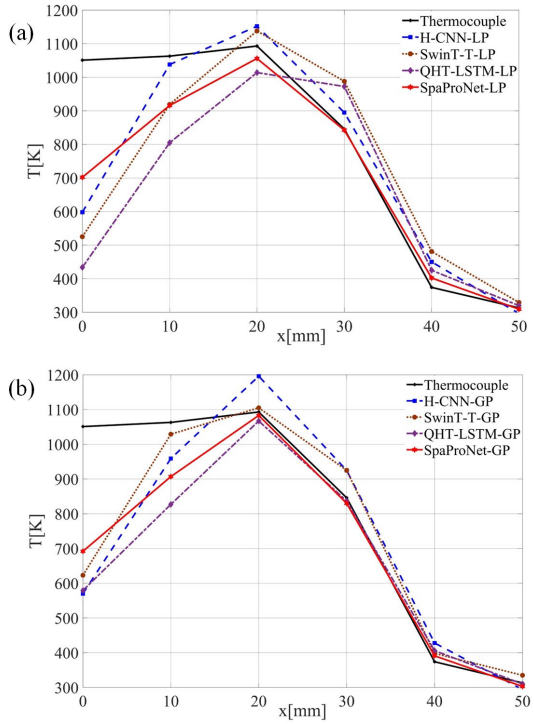

Fig. 9. Radial temperature retrieved by (a) locally prioritized and (b) globally prioritized data-driven algorithms, and comparison to the thermocouple measurements.

VII. Conclusion

A novel multiple-output imaging neural network, named as SpaProNet, is developed for TDLAST. The proposed network, for the first time, outputs two images of thermochemical parameters, temperature as an example in this work, with a) a hierarchical reconstruction with priority for the combustion zone and low spatial resolution for the background and b) a high-resolution reconstruction for the entire sensing region. Furthermore, the SpaProNet is trained by large eddy simulation of the real combustion fields, enabling learning of the hydrodynamics with minimum empirically determined prior.

The advantage of SpaProNet over the state-of-the-art data-driven methods has been validated by both numerical simulation with FDS and experiments with a 32-beam TDLAST sensor. This work takes an important step towards industrial combustion imaging with the objective of RoI-customized imaging. It offers not only a locally prioritized image for monitoring dynamic changes in the central combustion zone, but also a globally prioritized image of better-than-ever quality for analysis of heat dissipation and flame-air interactions. Applied with hydrodynamics-informed flow-field data, SpaProNet is expected to perform as an attractive diagnostic tool for dynamic and complex/harsh- scenario reactive flows in the foreseeable future. Our future efforts will also be made by integrating more explicit prior [10, 11] into deep-learning networks for generalizability-improved TDLAST in applications of reactive flow-field diagnosis.

References

[1] A. Romanowski, “Big data-driven contextual processing methods for electrical capacitance tomography,” *IEEE Transactions on Industrial Informatics*, vol. 15, no. 3, pp. 1609-1618, 2019.

[2] S. Liu, H. Wu, Y. Huang, Y. Yang, and J. Jia, “Accelerated structure-aware sparse Bayesian learning for three-dimensional electrical impedance tomography,” *IEEE Transactions on Industrial Informatics*, vol. 15, no. 9, pp. 5033-5041, 2019.

[3] S. Liu, Y. Huang, H. Wu, C. Tan, and J. Jia, “Efficient multitask structure-aware sparse Bayesian learning for frequency-difference electrical impedance tomography,” *IEEE Transactions on Industrial Informatics*, vol. 17, no. 1, pp. 463-472, 2021.

[4] H. McCann, P. Wright, K. Daun, et al.,“5 - Chemical Species Tomography,” in Woodhead Publishing Series in Electronic and Optical Materials, Industrial Tomography (Second Edition), Woodhead Publishing, pp. 155-205, 2022.

[5] C. Liu, L. Xu, “Laser absorption spectroscopy for combustion diagnosis in reactive flows: A review,” *Appl. Spectrosc. Rev.,* vol. 54, no. 1, pp. 1-44, 2019.

[6] W. Cai, C. F. Kaminski, “Tomographic absorption spectroscopy for the study of gas dynamics and reactive flows.” *Progress in Energy & Combustion Science*, vol. 59, pp. 1-31. 2017.

[7] K. Daun, S. Grauer, P. Hadwin, “Chemical species tomography of turbulent flows: Discrete ill-posed and rank deficient problems and the use of prior information.” *Journal of Quantitative Spectroscopy & Radiative Transfer*, vol. 172, pp. 58-74, 2016.

[8] C. Liu, Z. Cao, Y. Lin, L. Xu, and H. McCann, “Online cross-sectional monitoring of a swirling flame using TDLAS tomography,” *IEEE Trans. Instrum. Meas*., vol. 67, no. 6, pp. 1338-1348, 2018.

[9] Y. Bao, R. Zhang, G. Enemali, Z. Cao, B. Zhou, H. McCann, and C. Liu, “Relative entropy regularized TDLAS tomography for robust

temperature imaging," *IEEE Trans. Instrum. Meas*., vol. 70, Art no. 4501909, pp. 1-9, 2021.

[10] S. Grauer, P. Hadwin, T. Sipkens, et al. "Measurement-based meshing, basis selection, and prior assignment in chemical species tomography," *Optics express*, vol. 25, no. 21, pp. 22553-22566, 2017.

[11] J. Emmert, S. Wagner, K. Daun. "Quantifying the spatial resolution of the maximum a posteriori estimate in linear, rank-deficient, Bayesian hard field tomography," *Measurement Science and Technology*, vol. 32, no. 2, 2020.

[12] S. Grauer, J. Emmert, S. Sanders, et al. "Multiparameter gas sensing with linear hyperspectral absorption tomography," *Measurement Science and Technology*, vol. 30, no.10, Art no. 105401, 2019.

[13] J. Molnar, S. Grauer. "Flow field tomography with uncertainty quantification using a Bayesian physics-informed neural network," *Measurement Science and Technology,* vol. 33, no. 6, Art no. 065305, 2022.

[14] J. J. Rodríguez-Andina, M. D. Valdés-Peña and M. J. Moure, "Advanced features and industrial applications of FPGAs - A review," *IEEE Transactions on Industrial Informatics*, vol. 11, no. 4, pp. 853-864, 2015.

[15] J. Huang, H. Liu, J. Dai, and W. Cai, "Reconstruction for limited-data nonlinear tomographic absorption spectroscopy via deep learning," *J. Quant. Spectrosc. Radiat. Transf.*, vol. 218, pp. 187-193, 2018.

[16] J. Huang, J. Zhao, and W. Cai, "Compressing convolutional neural networks using POD for the reconstruction of nonlinear tomographic absorption spectroscopy," *Comput. Phys. Commun.*, vol. 241, pp. 33-39, 2019.

[17] Y. Jiang, J. Si, R. Zhang, G. Enemali, B. Zhou, H. McCann, and C. Liu, "CSTNet: A dual-branch convolutional network for imaging of reactive flows using chemical species tomography," *IEEE Trans. Neural Netw. Learn. Syst.*, 2022.

[18] J. Si, G. Fu, Y. Cheng, R. Zhang, G. Enemali, and C. Liu, "A quality-hierarchical temperature imaging network for TDLAS tomography," *IEEE Trans. Instrum. Meas*., vol. 71, Art no. 4500710 pp. 1-10, 2022.

[19] J. Si, A. Wang, Y, Cheng, "Temperature imaging network based on Swin Transformer for TDLAS tomography," *Proceedings of 14th International Conference on Digital Imaging Processing*., vol. 12342, pp. 796-803, 2022.

[20] R. Zhang, J. Si, G. Enemali, Y. Bao and C. Liu, "Spatially driven chemical species tomography with size-adaptive hybrid meshing scheme," *IEEE Sensors Journal*, vol. 22, no. 13, pp. 12728-12737, 2022.

[21] J. Si, G. Li, Y. Cheng, R. Zhang, G. Enemali and C. Liu, "Hierarchical temperature imaging using pseudoinversed convolutional neural network aided TDLAS tomography," *IEEE Trans. Instrum. Meas.*, vol. 70, pp. 1-11, 2021.

[22] A. Upadhyay, et al., "Tomographic imaging of Carbon Dioxide in the exhaust plume of large commercial aero-engines," *Applied Optics*, vol.61, no. 28, pp. 8540-8552, 2022.

[23] F. Song, J. Wu, Y. Zhu, H. Xu, Y. Li, Z. Yu. "Temperature field reconstruction method for aero engine exhaust using the colored background oriented Schlieren technology," *Optoelectronics Letters*, vol.18, no. 04, pp. 243-250, 2022.

[24] C. Liu, S. Tsekenis, N. Polydorides, H. McCann. "Toward customized spatial resolution in TDLAS tomography," *IEEE Sensors Journal*, vol. 19, pp. 1748-1755, 2019.

[25] C. Liu, L. Xu, Z. Cao, and H. McCann, "Reconstruction of axisymmetric temperature and gas concentration distributions by combining fan-beam TDLAS with onion-peeling deconvolution," *IEEE Trans. Instrum. Meas*., vol. 63, no. 12, pp. 3067-3075, 2014.

[26] J. Hu, L. Shen, and G. Sun. "Squeeze-and-excitation networks," *2018 IEEE/CVF Conference on Computer Vision and Pattern Recognition*, pp. 7132-7141, 2018.

[27] H. Hu, Q. Li, Y. Zhao and Y. Zhang, "Parallel deep learning algorithms with hybrid attention mechanism for image segmentation of lung tumors," *IEEE Transactions on Industrial Informatics*, vol. 17, no. 4, pp. 2880-2889, 2021.

[28] X. Zang, G. Li, and W. Gao, "Multi-direction and multi-scale pyramid in transformer for video-based pedestrian retrieval," *IEEE Transactions on Industrial Informatics*, 2022.

[29] A. Dosovitskiy, L. Beyer, A. Kolesnikov, D. Weissenborn, and N. Houlsby, "An image is worth 16x16 words: Transformers for image recognition at scale," arXiv: 2010.11929, 2020.

[30] K. B. McGrattan, et al., Fire dynamics simulator - Technical reference guide. National Institute of Standards and Technology, Building and Fire Research, 2000.

[31] S. V. Patankar, Numerical heat transfer and fluid flow. CRC press, 2018.

[32] Z. Liu, et al. "Swin transformer: Hierarchical vision transformer using shifted windows," *Proceedings of the IEEE/CVF International Conference on Computer Vision*, pp. 10012-10022, 2021.

[33] L Xu, C Liu, W Jing, et al. "Tunable diode laser absorption spectroscopy-based tomography system for on-line monitoring of two-dimensional distributions of temperature and H_2O mole fraction," *Review of Scientific Instruments*, vol. 87, no. 1, Art no. 013101, 2016.

[34] M. Li, L. Xu, and Z. Cao, "TDLAS tomography system for online imaging and dynamic process playback of temperature and gas mole fraction," *IEEE Trans. Instrum. Meas.,* vol.71, pp.1-10, 2022.

[35] A. Huang, Z. Cao, C. Wang, J. Wen, F. Lu and L. Xu, "An FPGA-based on-chip neural network for TDLAS tomography in dynamic flames," *IEEE Trans. Instrum. Meas.,* vol.70, pp.1-11, 2021.

[36] B. Lins, P. Zinn, R. Engelbrecht, and B. Schmauss, "Simulation-based comparison of noise effects in wavelength modulation spectroscopy and direct absorption TDLAS," *Appl. Phys. B*, vol. 100, no. 2, pp. 367-376, 2010.

[37] G. Enemali, R. Zhang, H. McCann and C. Liu, "Cost-effective quasi-parallel sensing instrumentation for industrial chemical species tomography," *IEEE Trans. Ind. Electron.*, vol. 69, no. 2, pp. 2107-2116, 2022.

[38] B. Liu, Q. Huang, and P. Wang, "Influence of surrounding gas temperature on thermocouple measurement," *Case Stud. Therm. Eng*., vol. 19, 100627, 2020.

Jingjing Si (Member, IEEE) has been with the School of Information Science and Engineering, Yanshan University, China, since 2002, where she is currently a Professor. Her current research interests include multimedia signal processing and machine vision.

Gengchen Fu received the M.S. degree in electronic science and technology in 2022 from Yanshan University. His research interest is focused on laser absorption spectroscopic tomography.

Xin Liu is currently pursuing the M.S. degree with the School of Information Science and Engineering, Yanshan University. His research interest is focused on laser absorption spectroscopic tomography.

Yinbo Cheng has been a Lecturer with the Ocean Collage, Hebei Agricultural University, China, since 2017. His current research interests include big data analytic, data mining, and machine learning.

Rui Zhang is currently pursuing the Ph.D. degree with the School of Engineering, University of Edinburgh. Her current research interest is focused on laser absorption spectroscopic tomography.

Jiangnan Xia is currently pursuing the Ph.D. degree with the School of Engineering, University of Edinburgh. His current research interests are on embedded system design and laser absorption spectroscopy.

Yalei Fu is currently a PhD student with the School of Engineering, University of Edinburgh. Her research interests are focusing on deep learning algorithm on LAS tomography and image reconstruction.

Godwin Enemali (Member, IEEE) has been a Lecturer in the Department of Electrical and Electronic Engineering, Glasgow Caledonian University, since 2022. His current research interests are on high-speed data acquisition system and laser absorption spectroscopy.

Chang Liu (Senior Member, IEEE) has been a Lecturer with the School of Engineering, University of Edinburgh, since 2018. His current research interests include laser absorption spectroscopy, active/passive optical tomography techniques and system design, and their applications to combustion diagnosis and environmental monitoring.